Additive Manufacturing 92 (2024) 104385

Contents lists available at ScienceDirect

Additive Manufacturing

journal homepage: www.elsevier.com/locate/addma

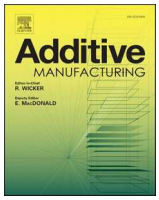

Aerosol jet 3D printing of gold micropillars and their behavior under compressive loads

Sanjida Jahan, Chunshan Hu, Bin Yuan, Sandra M. Ritchie, Rahul Panat *

Department of Mechanical Engineering, Carnegie Mellon University, Pittsburgh, PA 15213, USA

ARTICLE INFO

Keywords:
Aerosol jet 3D printing
Gold microstructure
Compressive behavior
Micropillar
Sintering

ABSTRACT

Three-dimensional (3D) gold microarchitectures such as micropillars, microwires, and microlattices are used in applications such as implantable biosensors, microelectronic circuits, and catalytic devices. Additive Manufacturing (AM) is being explored to create such structures as lithography is more suitable to fabricate 2D or planar architectures. In this work, we use Aerosol Jet (AJ) nanoprinting, a jetting-based AM technique, to demonstrate fabrication of gold micropillars via stacking of nanoparticles and sintering them at temperatures ranging from 300°C to 900°C. We first demonstrate that AJ printed 2D planar films and 3D micropillars exhibit a different grain size distribution, even if they are printed and sintered under identical conditions. This unusual observation indicates that specific AM technique and structures are important in determining their grain structure, which affects their mechanical behavior. The AJ printed 3D gold micropillars are fabricated with aspect ratios up to 10:1 and sintered from lower to higher temperatures, to yield porosities ranging from 15 % to 2 %, and average grain sizes from 25 nm to 1.7 μm, respectively. Micropillars sintered at lower temperatures exhibit a brittle behavior with higher yield strength despite having a higher porosity but with smaller grain sizes, and vice versa. These results indicate that the 3D geometry of AJ printed architectures dictates the grain size evolution, and hence the mechanical properties. Further, the grain size dominates over porosity in determining the micropillar deformation. These results provide important design guidelines for 3D printed microarchitected structures fabricated via jetting-based AM techniques.

1. Introduction

Microscale gold structures are used for applications such as microelectronics [1], high density brain-computer interfaces [2], sensors for biomolecules [3,4], and molecular sieves [5] because of their processability (ductility, and malleability), biocompatibility [6], and chemical inertness. Three-dimensional (3D) gold structures provide an additional advantage of increased surface area with high sensitivity for sensing and other surface-sensitive applications. Manufacture of microscale gold structures via conventional cleanroom-based technologies, while mature, involves time-consuming fabrication steps such as focused ion beam (FIB) milling from bulk Au [7], masking and etching [8], and dealloying [9] that lead to high resolution planar structures with low-aspect-ratio features in the z-direction. Recently, nanoparticle-based 3D printing techniques have allowed the fabrication of new device geometries, novel microstructures, and material combinations that were not possible to achieve via conventional cleanroom-based lithography. Extrusion printings, laser jetting, and inkjet printing have demonstrated building of 2D and 3D structures using gold nanoparticle inks [9–12]. Amongst several such methods, Aerosol Jet (AJ) 3D printing can create custom microarchitectures at a length scale down to 10 micrometers by deposition of nanoparticle-based inks [13]. In the case of a brain-computer interface, we need to reach different z-heights, inside the brain tissue to capture the neuronal firing patterns. This feat is not easily possible with micropillars made by FIB or lithography. Until recently, AJ printing was limited to 2D structures printed on planar and curved surfaces [14]. However, the printability has been extended significantly via the demonstration of complex 3D architectures that use droplet dynamics to stack and assemble nanoparticles in 3D space without any auxiliary support [15]. Through the removal of binders and solvents during sintering, controlled micro and/or nano structures can be achieved.

The mechanical properties of the gold microarchitectures play an important role in determining their end-use application. For example, micropillar-based brain-computer interfaces [2] record the action potentials throughout the 3D volume of the brain and can require their

* Corresponding author.
E-mail address: rpanat@andrew.cmu.edu (R. Panat).

https://doi.org/10.1016/j.addma.2024.104385
Received 2 February 2024; Received in revised form 8 August 2024; Accepted 26 August 2024
Available online 27 August 2024
2214-8604/© 2024 The Authors. Published by Elsevier B.V. This is an open access article under the CC BY-NC-ND license (http://creativecommons.org/licenses/by-nc-nd/4.0/).

penetration through dura, a thin sheet covering the brain, which has high toughness. In cases of implantable biomedical devices, the mechanical strength of microarchitectures determines the device durability and reliability. While the properties of bulk gold are well-known, they can change considerably for microscale structures made by additive manufacturing due to size effects [16] and the sintering-related voids/defects. Direct mechanical characterization of such structures to understand the microstructure-property relationship is the best way to assess their performance under practical use-conditions.

Mechanical properties of microarchitectures such as micropillars of various materials have been studied by several groups. Greer and Nix [16] showed that micro and nano-sized micropillars created by Focused Ion Beam (FIB) milling can exhibit a strength 50× of the bulk, which indicates a significant size effect. Cox and Dunand [17] created highly porous millimeter-sized gold structures which showed very low strength, which, in turn, was improved by annealing as the porosity decreased due to coarser grains. Our earlier work [18] has shown that silver micropillars fabricated by Aerosol Jet 3D printing, the material strength decreased with decreasing porosity and increasing grain sizes. In all cases, the direct compression study provided a good measure of their properties and reliability under application-relevant use-conditions.

This work is motivated by the fact that microscale gold structures are used in biomedical devices and other applications and understanding their structural integrity is important for the same. Specifically, we study the compression behavior of gold micropillars (100 μm diameter at 1:10 aspect ratio) made using the AJ 3D nanoprinting method. In this technique, gold nanoparticles were assembled in 3D space without any auxiliary support to create the micropillars followed by sintering under different temperatures to create a set of grain sizes and internal porosities which is different from aerosol jet printed 2D gold structures under identical conditions. Focused ion beam (FIB) was used to section the micropillars to get their internal porosities and grain sizes. We observe a transition from brittle to ductile behavior of the printed structures as the sintering temperature increases from 300 ℃ to 900 ℃. This behavior is then correlated with the internal microstructure of the micropillars which is the result of the additive manufacturing method. A two-phase porosity model is used to rationalize this mechanical behavior. Most importantly, our work indicates that the microstructure evolves differently in 3D printed architectures when compared to 2D films, providing guidelines for optimized 3D printing/sintering for various applications.

2. Materials and methods

2.1. Materials

Commercially available gold nanoparticle ink (UTDAu40, UT Dots Inc., Champaign, IL) was used to AJ print the micropillars. The gold nanoparticle size was 2–5 nm, the ink viscosity was 3 cP, and the particle loading was 40 wt%. The gold nanoparticle ink was dispersed in an organic non-polar solvent (also from UT Dots Inc., Champaign, IL) and aerosolized via ultrasonic energy during AJ printing. Gold 2D films and 3D micropillars were printed on alumina substrates with 96 % purity (ALN-101005S1, MTI Corp, Richmond, CA).

2.2. Aerosol jet (AJ) printing and sintering

Gold 2D films and 3D micropillars were printed using Aerosol Jet 3D printer (AJ300, Optomec Inc, Albuquerque, NM). To aerosolize the gold nanoparticle ink, an ultrasonic atomizer was used and a carrier gas, N_2, carried the aerosolized ink to the deposition head as shown in Fig. 1a. Inside the deposition head, the aerosol is focused by the sheath gas (also N_2) to the 150 μm diameter nozzle which can print at a resolution of 10–15 μm. A printing program was written in AutoCAD (AutoCAD 2015, Autodesk Inc., San Rafael, CA) using AutoLISP and converted to a "prg" file to be compatible with the printer software. In AutoLISP, the diameter of the micropillar and the number of layers to be printed were specified for 3D micropillars. The printing was carried out in a layer-by-layer manner. After printing 20 layers, the height of the micropillars was checked using an in-built alignment camera. Approximately 70 layers were printed to reach 1 mm height. Alumina substrates, approximately 1 cm × 1 cm in size, were cut using a diamond scriber pen, and plasma cleaned to remove impurities and contaminants from the surface. The substrate was placed and secured on the X-Y stage of the AJ printer as shown in Fig. 1a. A custom heating platform was used to locally heat the substrate to 300 °C so that the solvents and binder of the nanoparticle ink are burned off and the micropillars were partially sintered in-situ during printing. This was necessary to avoid bending of the micropillars as was observed in our earlier work [2,19]. The customized heating platform consisted of a heating element (PTC Heating Plate 110 V 140 W, FTVOGUE, Shenzhen, China), and a PID controller (CN745, Omega Engineering, Norwalk, CT). The temperature is monitored by a thermocouple (Digi-Sense Type K High-Temperature). The distance between the printer nozzle and the top surface of the printed structure was kept at ~2 mm. This was achieved by raising the deposition head by 100 μm after printing the same height for the micropillar. During printing, the carrier gas pressure and sheath gas pressure were 24 sccm and 60 sccm, respectively. The approximate time at 300 °C during printing experienced by each micropillar is about 40–60 minutes. After completion of printing, the gold micropillars were thermally sintered in a programmable oven (Neytech Vulcan furnace, Model 3–550, Degussa-Ney Dental Inc., Bloomfield, CT). Micropillars were sintered at 300, 400, 500, 600, 700, 800, or 900 °C for 4 hours. To reach the desired sintering temperature, a ramp rate of 1 °C/min was used, held at that temperature for 4 hours, and cooled down to the room temperature at a rate of 2 °C/min. Supplementary Figure S1 shows the sintering process curve for 400 °C sintering temperature. Fig. 1c and d show an AJ printed gold micropillar and its FIB cross-section, respectively, after sintering at 500 °C. Gold 2D films were printed in 2 mm × 2 mm dimension (three films per sintering temperature) on 15 mm × 15 mm alumina substrate at 300 °C platen temperature. To match the thermal histories with the 3D micropillars, these films were sintered at 300, 600 and 900 °C for 4 hours.

2.3. Compression test apparatus

Compression tests were performed using a custom uniaxial testing machine as shown in Fig. 1e. A flat aluminum platen was used to compress the micropillars at a strain rate of 0.5 mm/min. A 100 g load cell (Futek LSB200-FSH03870 FUTEK Advanced Sensor Technology Inc., Irvine, CA) was used to measure the force which was read by the data reader. The load cell was mounted on a linear stage (X-LSM025, Zaber Technologies Inc., Vancouver). A MATLAB (MathWorks, Natick, MA) script was used to record both the displacement and load simultaneously. A camera (Canon EOS Ti7 Rebel, Canon Corp., Tokyo, Japan) with a magnifying lens (model Tube TS-160, Infiniti Photo-Optical Company, Boulder, CO) recorded the displacement during compression which provided the global strain and the failure condition. At least 4–5 micropillars for each sintering temperature were used for the compression test.

2.4. Characterization

After printing and sintering the micropillars at different temperatures, microstructure was characterized by measuring grain size distribution, as well as pore sizes, and overall porosity. Microstructure was obtained by cross-sectioning micropillars using the focused ion beam (FEI Nova Nanolab 600 Dual Beam FIB, FEI Company, Hillsboro, OR) or FIB technique. A 2 μm thick Pt layer was deposited to protect the surface prior the FIB cut. During FIB, a course cut was performed using 15 nA ion beam current at 30 kV, followed by two polishing cuts using 0.3 nA and 0.1 nA ion beam currents at 30 kV. The same machine was used to

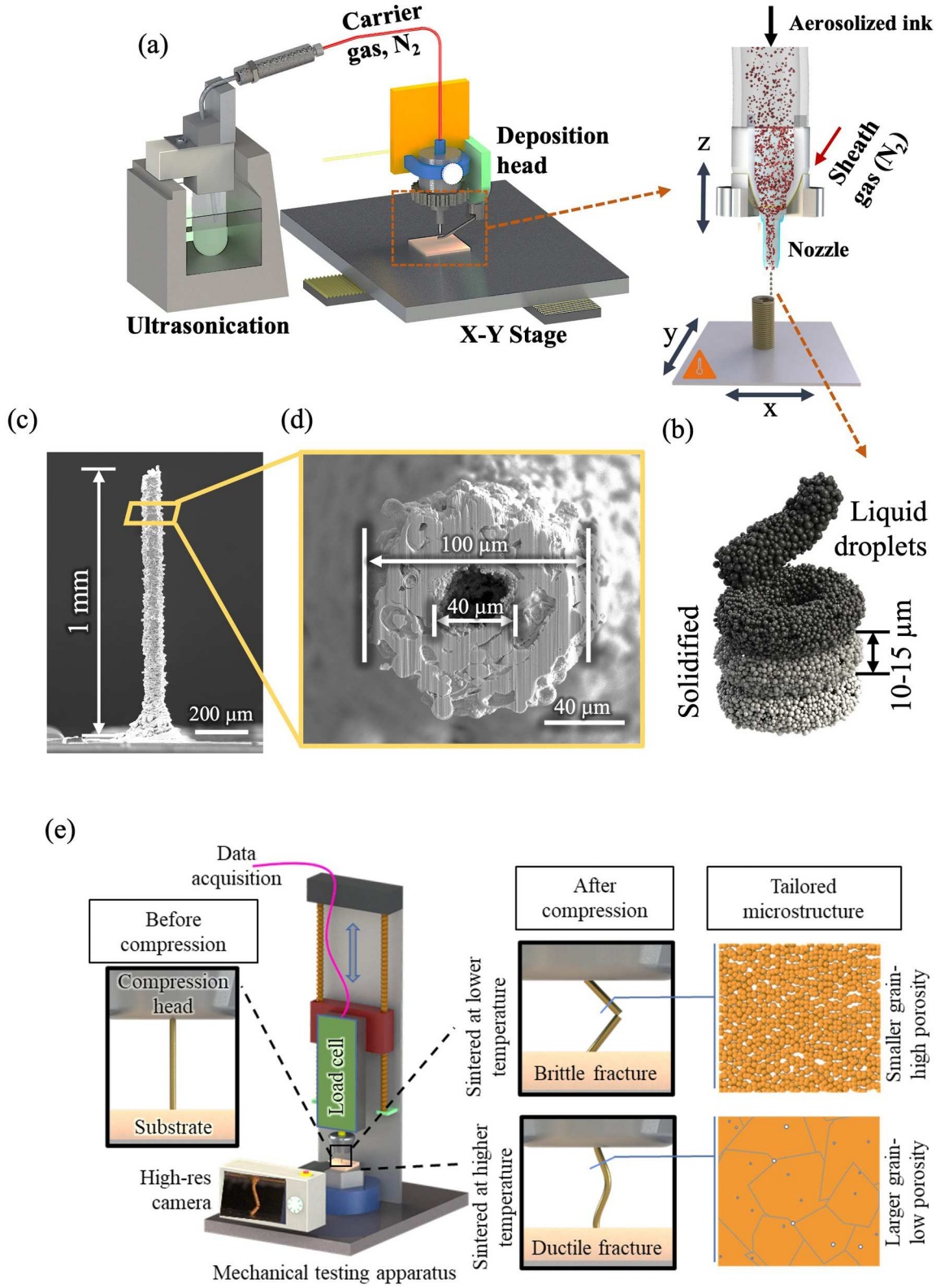

Fig. 1. 3D gold micropillars via AJ 3D printing process. (a) Aerosol generated via the ultrasonication of nanoparticle ink is carried to the nozzle by a carrier gas (N_2). Close-up schematic of the deposition head where nanoparticle ink is focused by sheath gas at a resolution of 10–15 µm through a 150 µm diameter nozzle. The deposition head can move in *z*-direction while the printing platen can move in *x*- and *y*-directions. 3D structure is made via layer-by-layer printing sequence and the interfacial adhesion between the solidified droplets and just-deposited liquid droplets as shown in (b). (c) SEM image of a single micropillar (1 mm tall) after printing and sintering at 500 °C used in this study. The sintering temperatures were varied from 300 °C to 900 °C. (d) Top view of a Focused Ion Beam (FIB) cross-section of the micropillar with dimensions. (e) A custom uniaxial compression test setup with load cell used for the compression test of the gold micropillars. A high-resolution camera recorded the nature of the failure under compressive loads. A data acquisition system collected the load data corresponding to the displacement. Due to the different sintering temperatures, gold micropillars had either brittle or ductile failure for lower temperature and higher temperature sintering, respectively. Schematic of cross-sectional micrographs showing that sintering of micropillars at lower temperature results in high porosity and small grain sizes and vice versa.

capture high resolution scanning electron micrographs (SEMs). The same cross-section method was followed for the grain size analysis of the 2D films.

Image processing software (ImageJ [20], NIH, Bethesda, MD) was used to obtain porosity observed in SEMs via a series of contrast and threshold adjustments. To determine the grain sizes, an ImageJ plugin, MorphoLibJ [21], was used to identify the grain boundaries. After pre-processing the images for noise, contrast, a tunable morphological filter (morphological gradient) was used to find the maxima. The watershed function was then used for segmenting contrasting structures. When the grains were segmented as individual structures, the particle analysis function was used to measure the individual grain area. The grain size here is defined as the diameter of a circle with the same area as the grain.

3. Results and discussion

3.1. Microstructure of the 2D AJ printed Gold film

Before studying the microstructure of AJ printed 3D micropillars, we studied the evolution of grain sizes in 2D films using high magnification cross-sectional SEM images. Supplementary Figure S2 shows the cross-sectional SEM images of the gold 2D films sintered at 300 °C, 600 °C, and 900 °C. From the TGA in Supplementary Figure S3, we found that the binder/solvent burnt off at 118 °C, confirming the binder/solvent removal while printing at higher temperature, i.e., 300 °C. The 2D films were then sintered for 4 hrs at 300 °C, 600 °C, and 900 °C, and their grain size distributions were analyzed using the cross-sectional SEM images.

To describe the grain size distribution, several empirical models can be used. In literature, the grain sizes are described by the Weibull distribution [22,23]. Another model is the log-normal distribution. However, for a steady-state grain growth, a Weibull distribution is shown to fit better than the log-normal distribution [24]. Another option is the normal distribution. This model, however, predicts a non-zero probability for negative grain sizes, which is physically impossible. We used a two-parameter Weibull distribution to represent the statistical distribution of the grain sizes in our work (as seen in SEMs). In addition, we also report the mean grain size (μ) as this metric is not captured by the Weibull distribution. Weibull distribution is a widely used parameter in describing grain size or pore size distribution in materials science [22, 25] and is represented by the curve,

$$f(d;\lambda,k) = \frac{k}{\lambda}\left(\frac{d}{\lambda}\right)^{k-1} e^{-(d/\lambda)^k} \quad , \tag{1}$$

where d is the grain size, k is the shape parameter, and λ is the scale parameter. The shape parameter k=3 represents a normal distribution, whereas k <3 represents a right-skewed distribution and vice versa. As seen in the grain size distribution shown in Fig. 2, and in Table 1, the values of k are more than 3, indicating left-skewed distributions. Scale parameter λ indicates the spread of the data; with larger λ representing a more extensive spread. In the present case λ appears to increase with the mean of the distribution - in fact, the ratio of scale parameter to the mean remains relatively constant for the grains (Table 1).

Table 1
Weibull parameters derived from the distribution of grain sizes measured from cross-sections of 2D gold films.

Sintering temperature (°C)	Weibull parameters			
	Scale parameter, λ	Arithmetic mean, μ (nm)	Scale parameter normalized by μ	Shape parameter, k
300	332.33	298	1.114	3.39
600	469.61	424	1.107	3.58
900	3565.51	3314	1.076	5.99

From the grain size distribution and the Weibull fits in Fig. 2, we can observe the increase in mean grain size, μ, from 298 nm, 424 nm, and 3.3 μm, for films sintered at 300 °C, 600 °C, and 900 °C, respectively. Further, the scale parameter, λ, increased 332.33–3565.51 with increasing sintering temperatures. A dramatic increase in mean grain size is observed from sintering temperature 600 °C to 900 °C. Twin structures are also observed at all sintering temperatures as seen in Supplementary Figure S2.

3.2. Microstructure of the 3D printed gold micropillars

As indicated before, porosity and grain size are expected to play a critical role in the mechanical behavior of AJ printed metallic structures. Fig. 3a, b, and c show representative SEM images of the FIB cross sections showing the grain size/structure and porosity for 3D micropillars Section 3.1 sintered at 300, 600 and 900 °C, respectively. Note that the curtaining effect caused by FIB sectioning in Fig. 3a(i), 3b(i), and 3c(i) is removed by the ImageJ software (corresponding original images are shown in Supplementary Figure S4). Fig. 3a(ii), 3b(ii), and 3c(ii) highlight the pores in red color identified by the technique described in 'Materials and Method' section, while Fig. 3a(iii), 3b(iii), and 3c(iii) show the corresponding grain boundaries and grain sizes. The porosity is seen to be evenly distributed over the section and the variations in pore sizes is very low for micropillars sintered at 300 °C (Fig. 3b-ii). Further, for 300 °C, the grain sizes are small as seen in Fig. 3b(iii). Average porosity for this temperature was found to be 14.5 ± 0.5 %. For the AJ printed micropillars sintered at 600 °C, we can see regional grain growth, which leads to different phases and twin boundaries (Fig. 3b-i) as often observed in literature [26], and irregularly distributed porosities at 6 ± 0.9 % (Fig. 3b-ii). It is noted that larger pores that are irregular in shape exist in regions where grain sizes are smaller, and smaller circular pores are primarily found in larger grain regions. This may be due to the fact that for the regions with large grains (that experienced grain growth), the voids are rearranged/displaced as the

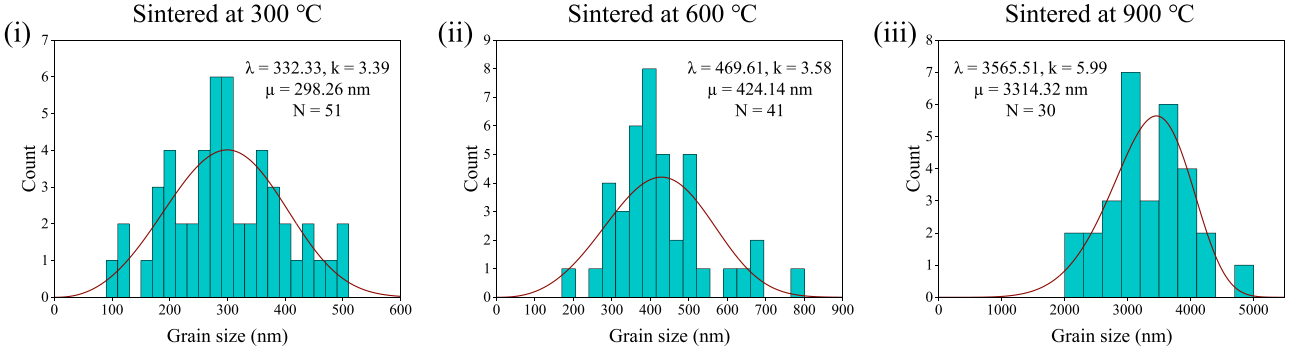

Fig. 2. Weibull distribution of the grain sizes of AJ printed 2D gold films. (i) Sintered at 300 °C, (ii) sintered at 600 °C, and (iii) sintered at 900 °C for 4 hrs.

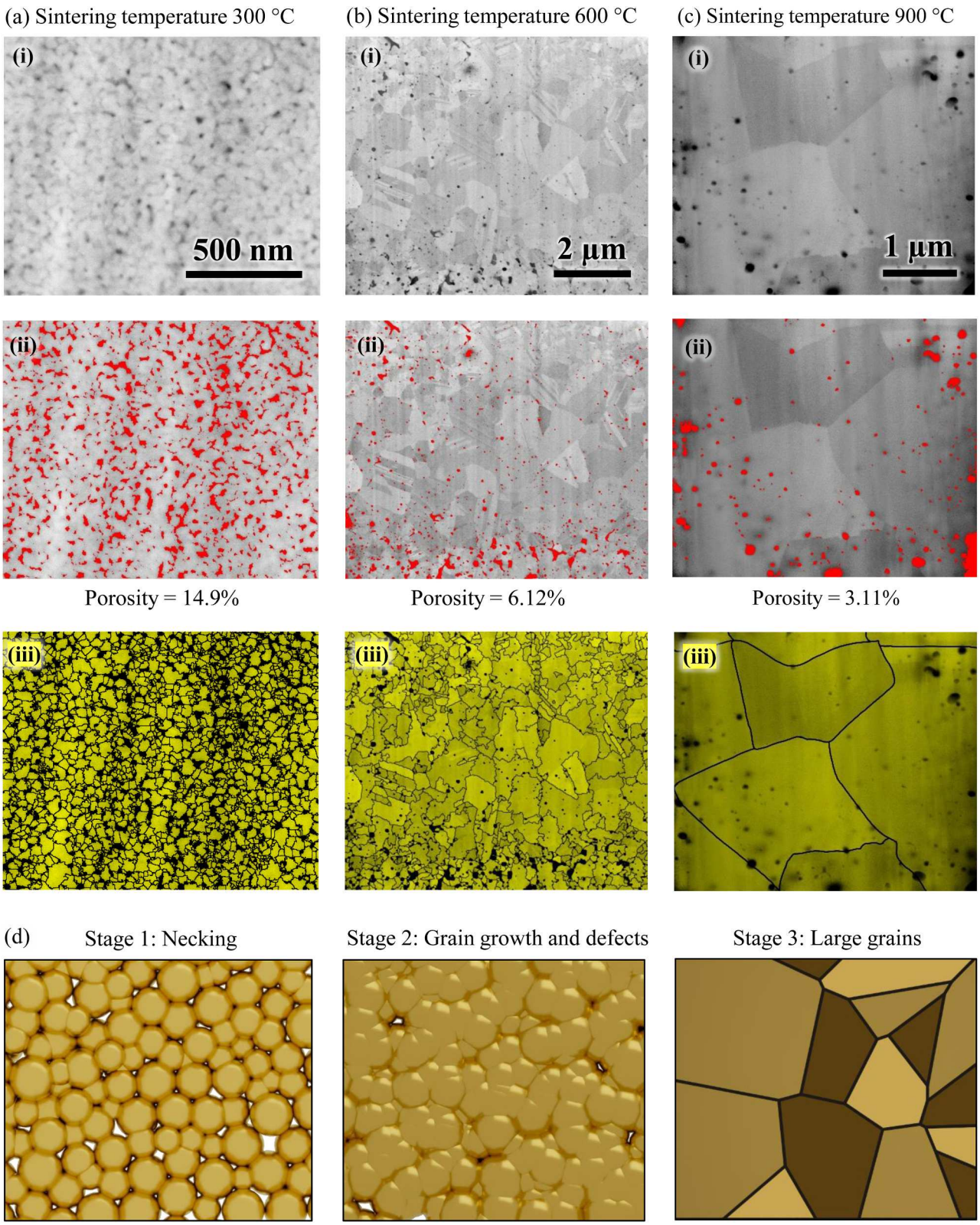

Fig. 3. Microstructure of AJ printed gold micropillars sintered at (a) 300 °C, (b) 600 °C, and (c) 900 °C. (i) Original SEM images, and the same images highlighting porosity (ii), and grain boundaries and hence grain sizes of micropillars sintered (iii). (d) Graphical representation of nanoparticle sintering and grain growth.

grains grew in size. Energetically, this may be understood as a reduction in surface areas associated with the pores during grain growth [27]. The grain sizes in Fig. 3b(iii) show bimodal distribution (discussed in detail later in this section). For 3D micropillars sintered at 900 °C, we observed low, unevenly distributed pores (Fig. 3c-ii) and larger grains (Fig. 3c-iii). Additional SEM images of FIB-cut sections of micropillars sintered at 300 °C are shown in Supplementary Figure S5. Representative SEMs, along with porosity and grain size analysis for samples sintered at additional temperatures are given in Supplementary Figures S6-S12. A schematic depicting the evolution of AJ printed grain structure during

sintering is shown in Fig. 3d. In stage 1, the AJ printed nanoparticles start to form necks, while in stage 2, some grain growth occurs, along with a reduction in porosity. Stage 3 shows fully coalesced grains with significant grain growth, minimal voids/defects, and clearly observed unique crystallographic orientations.

Fig. 4 shows the quantitative results extracted from the images in Fig. 3. Fig. 4a shows a comparison of the grain size spread for samples sintered at 300, 600 and 900 °C. For 3D micropillars with sintering temperatures of 300 °C, the grain sizes are well-defined and relatively small (< 100 nm), while for those sintered at 900 °C, the grains have a size of the order of a micron. The largest grain size recorded for 3D micropillars sintered at 900 °C was 4.4 μm. The spread in the grain size distribution for samples sintered at 600 °C, however, is significant, spanning from 10 nm to 1.5 μm. This may indicate that the rate of grain growth is nonuniform with the growth occurring such that the grain size to spread ratio remains constant. From Fig. 4b, we can observe a gradual increase in the mean grain size as a function of the sintering temperature. For example, for 300, 600, and 900 °C sintering temperatures, mean grain size was found to be 26 nm, 193 nm, and 1.7 μm respectively. The scale parameter, λ, also increased from 28.96 for sintering at 300 °C to 1925.30 for that at 900 °C. The irregular growth and coalescence of the particles in a closed space can be a reason for wider scale

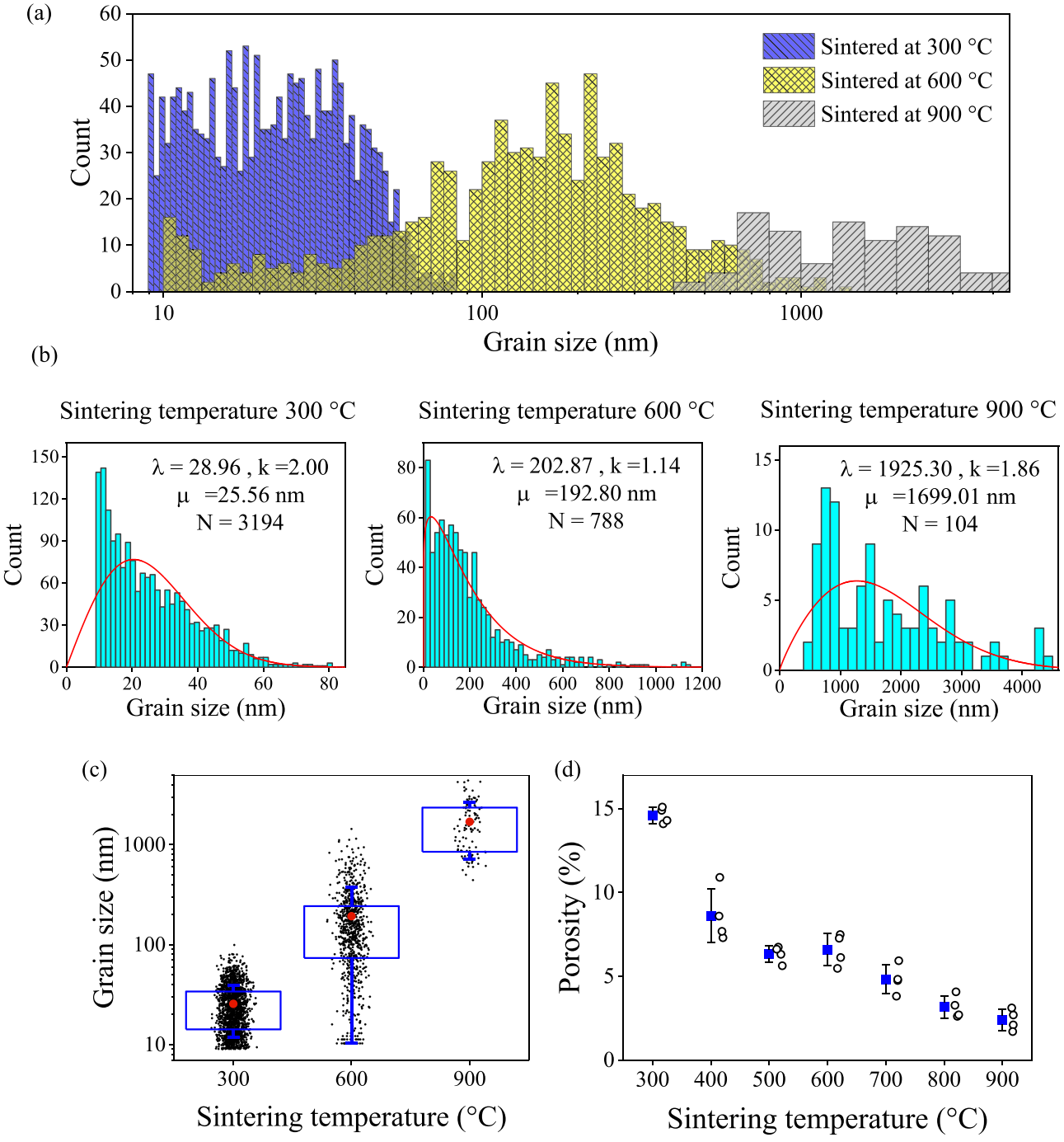

Fig. 4. Grain size and porosity of the AJ printed 3D gold micropillars sintered at different temperatures. (a) Combined histogram and (b) corresponding Weibull parameter fit of 3D gold micropillars sintered at 300 °C, 600 °C, and 900 °C. (c) Data in (a) and (b) plotted to highlight a wider distribution of grain sizes at the intermediate sintering temperature of 600 °C. (d) Porosity vs sintering temperature for all the samples studied in this work.

parameters at higher sintering temperatures. Table 2 gives the Weibull parameters for micropillars sintered at all the temperatures used in this work (i.e., including the images shown in Supplementary Figures S5-S11). Supplementary Figure S12 shows the grain size histograms and Weibull parameters for gold micropillars sintered at the remaining temperatures (i.e., 400 °C, 500 °C, 700 °C, and 800 °C). Fig. 4c shows the average grain size increment with sintering temperatures, which follows an exponential increase.

Comparing Fig. 2 with Fig. 4b, we observe that the mean grain sizes increase with increasing sintering temperature and are significantly higher for 2D gold films than for 3D micropillars. The mean grain size, μ, for 2D structures sintered at 300 °C, 600 °C, and 900 °C, is 298 ± 98 nm, 424 ± 124 nm and 3.3 ± 0.61 μm, respectively, whereas for 3D structures, these values are 26 ± 14 nm, 193 ± 183 nm, and 1.7 ± 0.98 μm, respectively. The p-value from the two-sample t-test is found to be < 0.001, which confirms the statistical significance in the difference in the grain sizes for 2D and 3D structures [28]. It is well known that for grain growth in films, the interface with the substrate and the top surface of the film suppress normal grain growth and promoting secondary or abnormal grain growth [29]. While developing specific models for grain growth in 3D microstructures are beyond the scope of this investigation, we establish that the microstructure of the 3D micropillars is markedly different than that for 2D film subjected to the same printing and sintering conditions. Since microstructure influences the mechanical properties of materials in the plastic regime (also observed later in this investigation), it is clear that properties of parts made by sintering-based AM processes need special consideration due to influence of geometry on the microstructure evolution.

A nonlinear decrease in porosity was observed with increasing temperature as shown in Fig. 4d. While a first principles model that correlates porosity with sintering temperatures of metals has not been established, a similar nonlinear dependence has been observed for the sintering of Titanium [30].

3.3. Compression behavior of the gold micropillars

Since the gold micropillars are being considered for applications such as Brain-Computer Interfaces (BCIs), or neural probes, it is imperative to understand their behavior under uniaxial compression (loading as they are inserted into the brain either with or without the dura layer) [2]. Several other applications such as 3D microelectronic interconnects and sensors would also benefit from such tests. Generally, for buckling to occur, the slenderness ratio, l/k, should be greater than $[2\pi^2 CE/S_y]^{1/2}$, where l is the length, k is the radium of gyration, C is ~1, E and S_y are the Young's modulus and yield strength of gold, respectively [31]. In our case, l/k is 37.13 and $[2\pi^2 CE/S_y]^{1/2}$ is between 14 and 28 which satisfies the condition for buckling. Since the pillar in Fig. 1c is slender, buckling is expected to be the primary mode of failure. For shorter columns, either pure compression or a mix of compression and buckling will dominate the failure mechanism. In other words, the load-displacement relationship obtained by direct compression will provide the behavior of these structures in a broad range of use conditions.

Table 2
Weibull parameters derived from the grain size measured from the cross-sectional SEMs.

Sintering temperature (°C)	Weibull parameters			
	Scale parameter, λ	Arithmetic mean, μ (nm)	Scale parameter normalized by μ	Shape parameter, k
300	28.96	26	1.133	2.00
400	51.97	46	1.132	2.33
500	201.46	179	1.124	1.72
600	202.87	193	1.052	1.14
700	402.76	355	1.135	2.15
800	932.04	821	1.135	1.86
900	1925.3	1699	1.133	1.86

Fig. 5a-c presents the force-displacement (stress-strain) curve and pillar condition at characteristic points on the graph for the gold micropillars sintered at 300, 600, and 900 °C respectively (data for micropillars sintered at all other temperatures is given in Fig. 6, and the videos of the compression tests are provided as Supplementary Movies S1 to S7). As the load increased, in all cases, we observed a linear response for low loads which is the elastic part. This elastic part is marked between point 1 and point 2, and the slope of this region is used to calculate the apparent elastic modulus of the micropillars. Note that due to possible misalignment of the axis of the pillars with the vertical direction, this slope may not indicate the intrinsic modulus of the structure and hence we will use the term 'apparent elastic modulus'. We can, however, calculate the Young's Modulus from the critical buckling load measured in experiments and compare it with the initial slope as done in this manuscript. For lower sintering temperature of 300 °C, the applied force reaches a peak load before fracture occurs in the mid-part of the pillars as shown in Fig. 5a. For pillars sintered at 600 °C shown in Fig. 5b, the mechanical response starts changing with increasing load as instead of a sudden failure, some ductile behavior is observed before fracture occurs.

Supplementary material related to this article can be found online at doi:10.1016/j.addma.2024.104385.

We observed a completely different deformation behavior for micropillars sintered at 900 °C (Fig. 5c). After the first and second linear parts (points 1–2 and then 2–3, respectively), the stress-strain curve drops with negative slope indicating buckling in the plastic region. After point 4, stress gradually drops to zero representing the characteristic ductile failure of bulk metal. In summary, AJ printed Au nanoparticle based micropillars sintered at low, medium, and high temperatures show brittle, ductile-brittle, and ductile behavior, respectively. The peak force, calculated yield strength, and the initial slope from the stress-strain curve for different sintering temperatures are shown in Table 3.

Fig. 6 summarizes the compression behavior of micropillars. Fig. 6a shows representative load-displacement curves for micropillars sintered at all the sintering conditions studied in this work. To be used as microelectrodes in a BCI, these microelectrodes will undergo axial loading while inserting into soft tissue, e.g., brain, spinal cord etc. In our previous work, a phantom brain, agarose was used to determine the insertion force per micropillar which was found to be between 0.1 and 1 mN [2]. From Table 3 and Fig. 6a, we can observe that the critical buckling force for such micropillars is more than 70 mN which is more than one order of magnitude higher than that required for insertion in the soft issue, confirming the suitability of the our micropillars as microelectrodes in BCIs for mechanical integrity. We observe that for the 3D micropillars sintered at temperatures from 300 to 500 °C, an initial linear elastic regime followed by a sudden drop in load is observed, exhibiting little plastic deformation. This brittle behavior also has an interesting feature that the load to failure at 400 °C is considerably higher than that for 300 or 500 °C. The micropillar sintered at 600 °C shows two distinct regions when the load goes up. This behavior, discussed earlier in this section, points to a combination of elastic and plastic deformation, where a more brittle behavior is observed. For micropillars sintered at 700–900 °C, all the samples showed a nonlinear behavior, indicating a plastic (or ductile) behavior. The maximum yield strength was found at 400 °C and the value is comparable to the compressive yield strength of bulk gold (20–205 MPa at 2 % strain [32]).

We further analyzed our data in two different ways. First, the initial loading slope, E_s, was calculated by measuring the slope of each curve during the initial linear region of the load-displacement plots in Fig. 6a. Second, the Elastic modulus (E_b) is estimated using the classic Euler buckling theory where the critical buckling load is equated with the peak force at the end of the first linear region. We use the classical

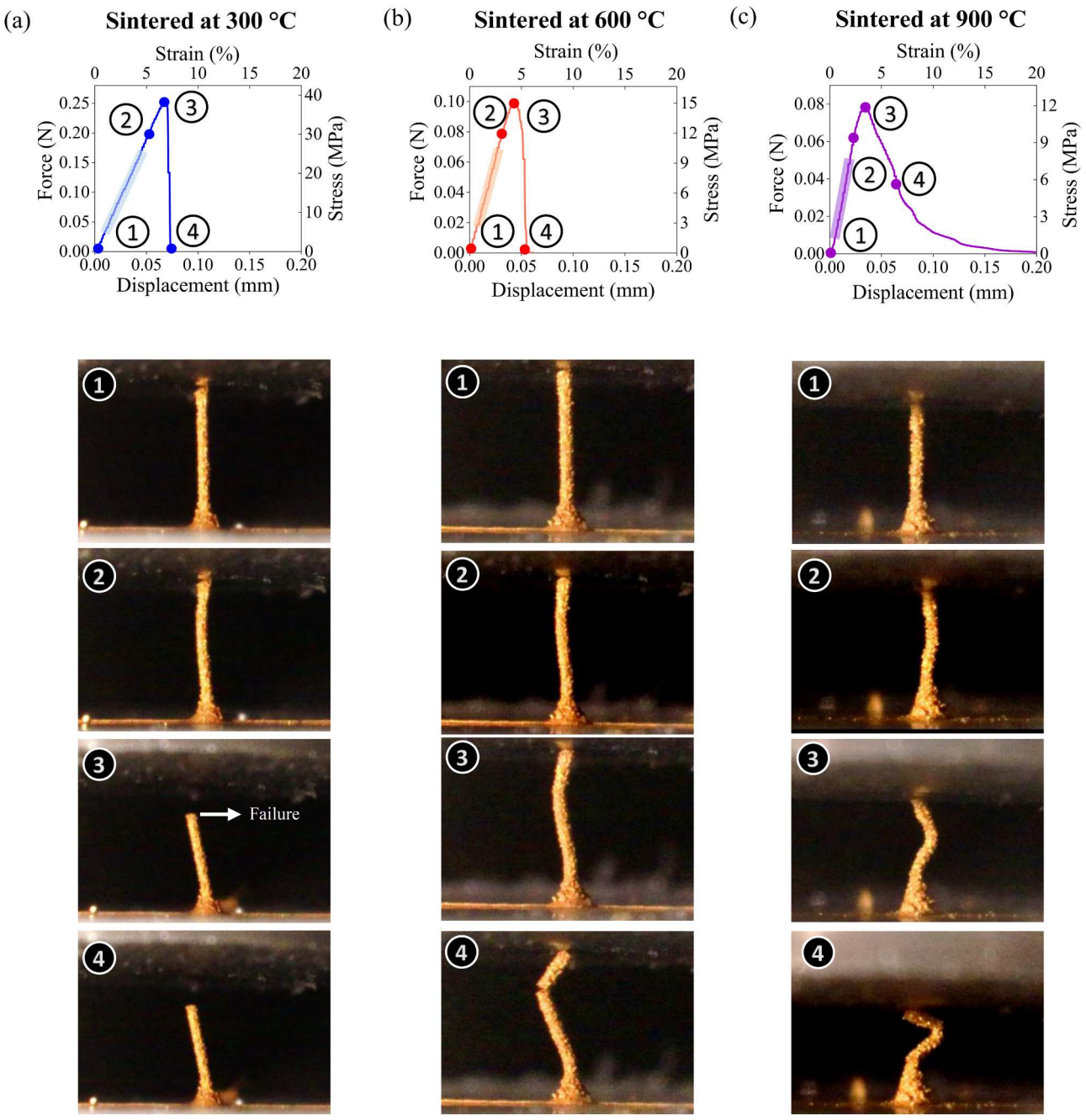

Fig. 5. Force-displacement (stress-strain) plot from the compression tests of gold micropillars sintered at (a) 300 °C, which shows brittle failure, (b) 600 °C, which shows brittle-ductile failure and, (c) 900 °C, which shows ductile failure. Four pictures depict the marked points on the plot captured from the video. The initial elastic region is marked as a shaded area in the plots.

formula, $P_{cr} = \pi^2 EI/(Cl)^2$, where I is the area moment of inertia of the structure, l is the column length, and C is the effective length factor which is determined by the end conditions of the column/loading structure. In our experiment system, since the pillars are fixed on the substrate and there is no relative sliding at the other end during compression (as confirmed by compression videos), we take $C = 0.7$ [33]. Fig. 6b and c show the apparent Elastic moduli under different sintering temperatures (E_s and E_b) calculated using these two techniques. From Fig. 6c, it is clear that E_s reaches at maximum for 400 °C and then drops to the minimum for 800 °C. With further increase of the sintering temperature, E_s is nearly constant with an average of 330 MPa. We note that elastic theory does not predict grain-size dependence of elastic modulus of materials. These results show that in spite of having a higher porosity, the samples at lower sintering temperature behave in a 'brittle' manner; while samples sintered at higher temperature, in spite of having lower porosity, exhibit a more compliant behavior. This behavior is discussed in the next section in the context of a two-phase porosity model.

3.4. Discussion

The results presented in the previous sections demonstrate that the stress-strain behavior of AJ printed micropillars as measured by elastic modulus, peak/buckling force, and strain to failure, is a strong function of their microstructure. This microstructure, in turn, is a function of the micropillar sintering conditions and whether the part has a 3D shape (vs

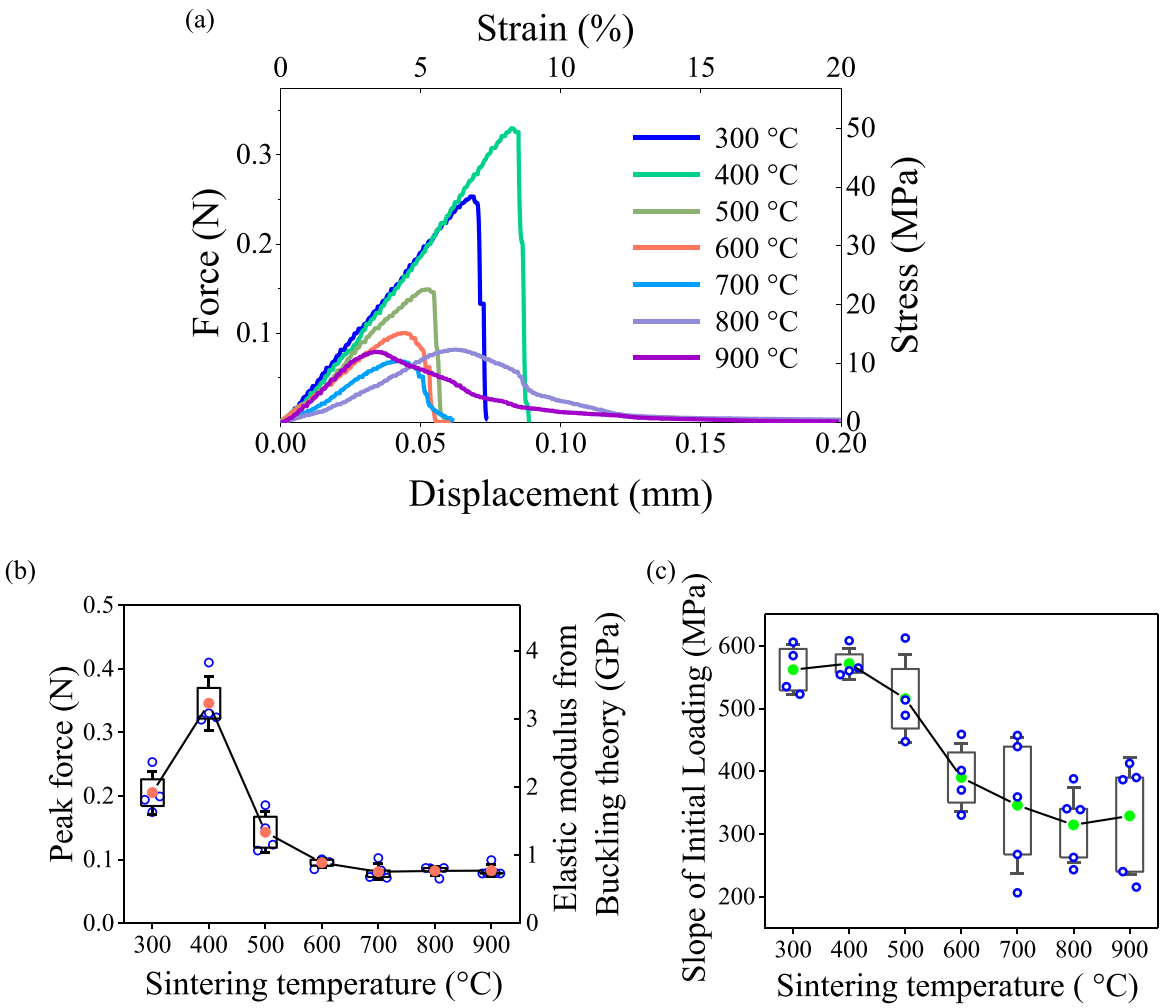

Fig. 6. Buckling behavior of the 3D printed gold micropillars. (a) Representative force-displacement and stress-strain plot of micropillars sintered at 300 °C to 900 °C under compressive load, (b) Peak force and elastic modulus derived from the Euler's buckling model from each test plotted against sintering temperature, (c) Slope of the stress-strain curve at lower strain where the slope is linear plotted against the sintering temperature.

Table 3
Mechanical properties of micropillars sintered under different conditions.

Sintering temperature (°C)	Peak force (mN)	Stress at peak force (apparent yield strength) (MPa)	Slope of Stress-Strain plot in elastic regime, E_s (GPa)	Young's modulus calculated using buckling theory, E_b (GPa)
300	205.2 ± 29.2	31.1 ± 4.4	0.56 ± 0.03	2.13 ± 0.30
400	345.8 ± 37.1	52.4 ± 5.6	0.57 ± 0.02	3.59 ± 0.39
500	143.0 ± 27.7	21.7 ± 4.2	0.52 ± 0.06	1.48 ± 0.29
600	95.1 ± 6.2	12.4 ± 2.6	0.33 ± 0.04	0.83 ± 0.26
700	71.4 ± 15.7	8.8 ± 3.4	0.35 ± 0.10	0.74 ± 0.16
800	82.2 ± 6.5	11.6 ± 1.2	0.31 ± 0.05	0.85 ± 0.07
900	82.5 ± 8.3	11.5 ± 0.5	0.33 ± 0.08	0.86 ± 0.09

a film made under identical conditions). Although classical elasticity predicts no dependence of elastic modulus (and hence, for example, critical elastic buckling load) of a material on the grain size, our results show otherwise. This is not surprising given that we have a presence of porosity in the material and may have local plastic deformation even prior to the initial buckling event. Such dependence of modulus on grain size in the presence of porosity has been discussed in literature, including our previous work [17,34–37].

From the Hall-Petch relationship [38,39], the decreasing grain sizes increase the yield strength, and the material behavior is more akin to 'brittle' manner. On the contrary, with increasing porosity, a rule-of-mixture approximation would predict a decrease in the effective elastic modulus with porosity (i.e., an effective softening). Clearly, the effective elastic modulus for our micropillars increased when sintering temperature is increased from 300 to 400 °C but decreased with increasing sintering temperature. As sintering temperature is directly proportional to the average grain size, increasing grain size decreased the elastic modulus for 400–900 °C sintering temperature. This also correlated with a reduction in the internal porosity for the micropillars with the sintering temperature. Note that Hamid et al. [37] carried out discrete dislocation dynamic simulations for the behavior of the silver micropillar under compression. They concluded that both grain size and porosity can affect the mechanical behavior of the micropillars. Note also that due to the interplay between grain size and porosity, the Hall-Petch relationship cannot be directly applied to our results.

To rationalize this behavior, we use a two-phase microstructure model where the grains and the pores are considered as two phases of the system [40]. Note that this model is semi-empirical and hence is used to rationalize our findings. If we make the assumption of equiaxed

particles and random distribution of the pores, we can write the following equations [41]:

$$E_{eff} = E_0 f_c \tag{2}$$

$$f_c = \frac{(1-P)^2 R}{P + (1-P)R} \tag{3}$$

$$R = \frac{d_P}{d_G} \tag{4}$$

where, E_{eff} is the effective elastic modulus of the porous material, E_0 is the elastic modulus of the nonporous or bulk material, P is the porosity fraction, d_P and d_G are the mean diameter of the pores and the grains, respectively. Fig. 7a plots the average grain sizes and pore sizes for the micropillars for each of the sintering temperatures. This gives R and f_c as a function of the sintering temperatures. The variation of R with the sintering temperature is shown in Fig. 7b. The E_{eff}/E_0 as a function of porosity for the micropillars sintered at temperatures from 300 to 900 °C is plotted in Fig. 7c. Each curve corresponds to the R value shown in Fig. 7b for a given sintering temperature. From Fig. 7c, E_{eff}/E_0 increases with decreasing porosity. This effect is dominant for micropillars sintered at higher temperatures (and lower R values) having larger grain sizes (and low porosity). On the contrary, smaller grain size can have larger R and higher E_{eff}/E_0 at low porosity. In our study, we found that micropillars sintered at 300 °C have lower strength than micropillars sintered at 400 °C (Fig. 6b and c). As the porosity decreased significantly from 300 to 400 °C (Fig. 4d), it led to an increase in the effective modulus of the micropillar. Thus, using the two-phase model, we can explain the rise in the material strength from 300 to 400 °C and the drop of the material strength from 400–900 °C.

These observations clearly indicate that the dominant factor determining the mechanical behavior of the micropillars is the grain size rather than the porosity. In other words, as the grain size reduces, the dislocations in the system have difficulty passing through the grain boundaries, leading to an increase in the strength during compression, and a lower failure strain. This is despite the samples having a higher porosity. For samples with larger grains, though, the volume occupied by the grain boundaries is lower, leading to an easier passing of the

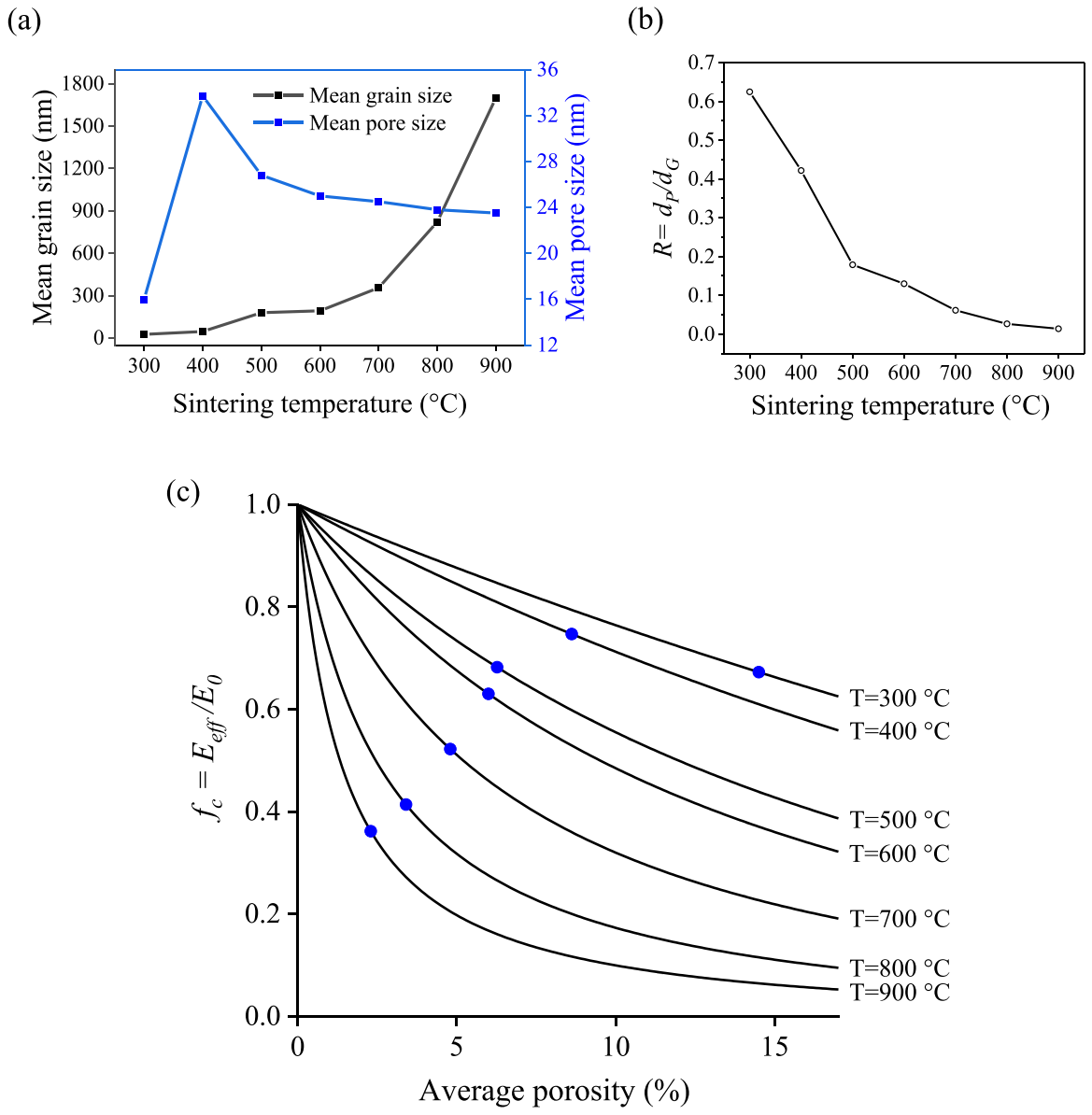

Fig. 7. Porosity and grain size effect on material strength using two-phase mechanical model. (a) Grain size and pore size vs. sintering temperature, (b) average pore and grain size ratio, R, as a function of the sintering temperature, and (c) Relative elastic modulus as a function of porosity based on two-phase model.

dislocations during plastic deformation and a 'ductile' behavior characterized by a high strain-to-failure (even under a very low porosity). We note that prior work by Zbib and coworkers [42] has shown that defects can actually act as pinning locations for dislocation motion. In other words, contrary to expectation, regularly distributed micropores can actually strengthen a solid under deformation. If the pores are larger, however, they can act as crack initiation sites and degrade the strength of the crystal. In-situ Transmission Electron Microscopy (TEM) observations can reveal the exact role of pores and grain sizes of our system. In absence of such operando microscopy, however, our load-displacement data indicates that the uniformly distributed high porosity has led to a higher strength of the crystal. Lastly, we recognize that in our work the grain size and porosity are not independently varied due to experimental limitations. A manufacturing technique where both can be independently varied can shed a clearer light on this exciting phenomenon. Clearly, additional research is needed to reveal the nuances of this mechanism.

The data presented in this work leads to the conclusion that AJ printing and sintering is a viable fabrication route to create microscale gold 3D structures for device applications. By varying the sintering conditions, the engineering stress when the micropillars buckle/break varies from about 10–50 MPa. This level of stress is sufficient for various applications. For example, for implantable brain-computer interfaces, the load to insert the micropillars in the brain tissue for comparable sized micropillars is significantly lower than that in Fig. 6a [2].

4. Conclusion

In this work, we demonstrate the fabrication of gold micropillars using Aerosol Jet 3D nanoprinting technique. The microstructure of the 2D films and 3D micropillars printed and sintered at identical condition is examined in detail using cross-sectional SEMs. Compression tests of the micropillars are carried out to understand their behavior in use conditions. The behavior is correlated with the microstructure, which is unique toprinting techniques. The main conclusions of the work are:

(i) AJ printing and sintering is a feasible fabrication technique to create 3D gold micropillars with a strength of up to 50 MPa for various applications.
(ii) The geometry of the AJ printed 3D microarchitectures creates a different sintering behavior when compared to AJ printed 2D films subjected to identical thermal histories. We thus conclude that the mechanical behavior of parts made using sintering-based AM can be strongly influenced by the 3D part geometry, in addition to the sintering conditions.
(iii) The sintering conditions for the 3D micropillars affect their microstructure and mechanical properties significantly. For lower sintering temperatures of 300 – 500 °C, the micropillars exhibited relatively high porosity (7 %-15 %), with small average grain sizes (50–200 nm). For higher sintering temperatures of 700–900 °C, the micropillars showed low porosity (<5 %), and higher grain sizes (350 nm – 1.8 μm). The microstructure of samples sintered at 600 °C had regions of smaller and larger grain sizes indicating a transition in microstructure.
(iv) The microstructure of the 3D micropillars sintered at different temperatures led to a remarkably different behavior under compression. Specifically, contrary to expectations, the micropillars with lower porosity (but larger grains) showed a highly ductile behavior with lower peak force; and vice versa. In addition, a higher peak force was observed for samples sintered at 400 °C, compared to those sintered at 300 and 500 °C. These observations can be well explained by a two-phase mechanical model for deformation, which considers the pores and the grains as two distinct phases undergoing deformation.
(v) The grain size dominates over the porosity in determining the mechanical behavior of the AJ printed and sintered gold micropillars. The sintering condition thus becomes a powerful input parameter that can modulate the behavior of the micropillars.

CRediT authorship contribution statement

Chunshan Hu: Visualization, Validation, Investigation. **Bin Yuan:** Investigation. **Sandra Ritchie:** Investigation. **Rahul Panat:** Writing – review & editing, Supervision, Resources, Project administration, Methodology, Funding acquisition, Conceptualization. **Sanjida Jahan:** Writing – review & editing, Writing – original draft, Methodology, Formal analysis, Data curation.

Declaration of Competing Interest

The authors declare that there is no conflict of interest regarding the publication of this article.

Data Availability

Data will be made available on request.

Acknowledgments

The authors acknowledge partial support from the NIH (grants# RF1NS110483) and NSF CMMI award #2328678. We acknowledge use of the Materials Characterization Facility (MCF) at Carnegie Mellon University supported by grant MCF-677785. Work performed in the University of Pittsburgh Nanofabrication and Characterization Core Facility (RRID:SCR_05124) and services and instruments used in this project were graciously supported, in part, by the University of Pittsburgh.

Appendix A. Supporting information

Supplementary data associated with this article can be found in the online version at doi:10.1016/j.addma.2024.104385.

References

[1] Y.J. Yun, et al., Highly conductive and environmentally stable gold/graphene yarns for flexible and wearable electronics, Nanoscale 9 (32) (2017) 11439–11445.
[2] M.S. Saleh, et al., CMU Array: A 3D nanoprinted, fully customizable high-density microelectrode array platform, Sci. Adv. 8 (40) (2022) eabj4853.
[3] M.A. Ali, et al., Sensing of COVID-19 antibodies in seconds via aerosol jet nanoprinted reduced-graphene-oxide-coated 3D Electrodes, Adv. Mater. 33 (7) (2021) 2006647.
[4] C. Yu, J. Irudayaraj, Multiplex biosensor using gold nanorods, Anal. Chem. 79 (2) (2007) 572–579.
[5] M. Wirtz, et al., Molecular sieving and sensing with gold nanotube membranes, Chem. Rec. 2 (4) (2002) 259–267.
[6] M. Seiti, P.S. Ginestra, E. Ferraris, Aerosol Jet Printing of 3D biocompatible gold nanoparticle-based micro-structures. Selected Topics in Manufacturing: Emerging Trends from the Perspective of AITeM's Young Researchers, Springer, 2023, pp. 19–34.
[7] J.R. Greer, W.C. Oliver, W.D. Nix, Size dependence of mechanical properties of gold at the micron scale in the absence of strain gradients, Acta Mater. 53 (6) (2005) 1821–1830.
[8] D. Sánchez-Molas, et al., High aspect-ratio, fully conducting gold micropillar array electrodes: silicon micromachining and electrochemical characterization, J. Phys. Chem. C. 116 (35) (2012) 18831–18846.
[9] C. Zhu, et al., Toward digitally controlled catalyst architectures: hierarchical nanoporous gold via 3D printing, Sci. Adv. 4 (8) (2018) eaas9459.
[10] Brown, M.A., et al., *Direct laser writing of 3D electrodes on flexible substrates*. bioRxiv, 2022.
[11] M. Zenou, A. Sa'Ar, Z. Kotler, Laser jetting of femto-liter metal droplets for high resolution 3D printed structures, Sci. Rep. 5 (1) (2015) 1–10.
[12] S.H. Ko, et al., Metal nanoparticle direct inkjet printing for low-temperature 3D micro metal structure fabrication, J. Micromech. Microeng. 20 (12) (2010) 125010.
[13] M.S. Saleh, et al., 3D printed three-dimensional metallic microlattices with controlled and tunable mechanical properties, Addit. Manuf. 39 (2021) 101856.

[14] N.J. Wilkinson, et al., A review of aerosol jet printing—a non-traditional hybrid process for micro-manufacturing, Int. J. Adv. Manuf. Technol. 105 (11) (2019) 4599–4619.
[15] M.S. Saleh, C. Hu, R. Panat, Three-dimensional microarchitected materials and devices using nanoparticle assembly by pointwise spatial printing, Sci. Adv. 3 (3) (2017) e1601986.
[16] J.R. Greer, W.D. Nix, Nanoscale gold pillars strengthened through dislocation starvation, Phys. Rev. B 73 (24) (2006) 245410.
[17] M.E. Cox, D.C. Dunand, Bulk gold with hierarchical macro-, micro-and nano-porosity, Mater. Sci. Eng.: A 528 (6) (2011) 2401–2406.
[18] M.S. Saleh, et al., Polycrystalline micropillars by a novel 3-D printing method and their behavior under compressive loads, Scr. Mater. 149 (2018) 144–149.
[19] S.M. Ritchie, et al., Shape distortion in sintering results from nonhomogeneous temperature activating a long-range mass transport, Nat. Commun. 14 (1) (2023) 1–11.
[20] C.A. Schneider, W.S. Rasband, K.W. Eliceiri, NIH Image to ImageJ: 25 years of image analysis, Nat. Methods 9 (7) (2012) 671–675.
[21] D. Legland, I. Arganda-Carreras, P. Andrey, MorphoLibJ: integrated library and plugins for mathematical morphology with ImageJ, Bioinformatics 32 (22) (2016) 3532–3534.
[22] C. Wang, G. Liu, On the stability of grain structure with initial Weibull grain size distribution, Mater. Lett. 57 (28) (2003) 4424–4428.
[23] Y. Sun, G. Liu, C. Wang, On the grain size distributions obtained from different grain growth simulation techniques, J. Mater. Sci. 39 (7) (2004) 2553–2556.
[24] W. Fayad, C. Thompson, H. Frost, Steady-state grain-size distributions resulting from grain growth in two dimensions, Scr. Mater. 40 (10) (1999) 1199–1204.
[25] P. Rosin, Laws governing the fineness of powdered coal, J. Inst. Fuel (7) (1933) 29–36.
[26] C. Cason, et al., Effect of microstructure and residual stresses, generated from different annealing and deformation processes, on the corrosion and mechanical properties of gold welding alloy wires, Gold. Bull. 48 (2015) 135–145.
[27] G. Tomandl, P. Varkoly, Three-dimensional computer modeling of grain growth and pore shrinkage during sintering, Mater. Chem. Phys. 67 (1-3) (2001) 12–16.
[28] C. Lin, C. Berndt, Statistical analysis of microhardness variations in thermal spray coatings, J. Mater. Sci. 30 (1995) 111–117.
[29] C.V. Thompson, Grain growth in thin films, Annu. Rev. Mater. Sci. 20 (1) (1990) 245–268.
[30] D. Yang, et al., Influences of sintering temperature on pore morphology, porosity, and mechanical behavior of porous Ti, Mater. Res. Express 8 (10) (2021) 106519.
[31] Shigley, J.E., L.D. Mitchell, and H. Saunders, *Mechanical engineering design*. 1985.
[32] Saviëtiskii, E.M., *Handbook of precious metals*. 1989.
[33] R.G. Budynas, J.K. Nisbett, Shigley's Mechanical Engineering Design, McGraw-Hill, New York, 2011. Vol. 9.
[34] H.S. Kim, M.B. Bush, The effects of grain size and porosity on the elastic modulus of nanocrystalline materials, Nanostruct. Mater. 11 (3) (1999) 361–367.
[35] M. Becton, X. Wang, Grain-size dependence of mechanical properties in polycrystalline boron-nitride: a computational study, Phys. Chem. Chem. Phys. 17 (34) (2015) 21894–21901.
[36] M. Sadeq Saleh, et al., Polycrystalline micropillars by a novel 3-D printing method and their behavior under compressive loads, Scr. Mater. 149 (2018) 144–149.
[37] M. Hamid, et al., Modeling of porosity and grain size effects on mechanical behavior of additively manufactured structures, Addit. Manuf. 38 (2021) 101833.
[38] E. Hall, The deformation and ageing of mild steel: III discussion of results, Proc. Phys. Soc. Sect. B 64 (9) (1951) 747.
[39] N. Petch, The cleavage strength of polycrystals, J. Iron Steel Inst. 174 (1953) 25–28.
[40] A. Boccaccini, Z. Fan, A new approach for the Young's modulus-porosity correlation of ceramic materials, Ceram. Int. 23 (3) (1997) 239–245.
[41] Underwood, E., *Quantitative Stereology*,(*Addison-Wesley, Reading, MA*. 1970), 1970.
[42] T. Diaz de la Rubia, et al., Multiscale modelling of plastic flow localization in irradiated materials, Nature 406 (6798) (2000) 871–874.